ADVANCED FUNCTIONAL MATERIALS
www.afm-journal.de

Cell Migration and Breast Cancer Metastasis in Biomimetic Extracellular Matrices with Independently Tunable Stiffness

*Jyothsna Vasudevan, Chwee Teck Lim, and Javier G Fernandez**

The mechanics of the extracellular matrix (ECM) have long been known to have important implications for cancer metastasis and cell migration. An atypical increase in tumor ECM stiffness occurs because of the heightened deposition of ECM proteins and increased crosslinking density of fibrillar collagen. This tissue stiffening is an essential contributor to disease progression; however, its precise role remains mostly unidentified. Recent advances in synthetic ECM analogs have enabled the concurrent exploration of the effects of crosslinking density, ligand concentrations, matrix stiffness, and pore sizes on tumor cell invasion. However, this convolution of parameters prevents an understanding of the independent contribution of each separate parameter to tumorigenesis. Here, the use of a precisely adjusted degree of methacryloyl substitution in gelatin-based hydrogel to capture the heterogeneity in cancer cell behavior in response to matrix stiffness is characterized and demonstrated. The proposed ECM model and biomimetic stiffening mechanism are used to produce complex 3D environments with physiological characteristics and independently tunable stiffness. Two populations of invasive and noninvasive human breast adenocarcinoma are embedded in these matrices and monitored by computer vision, enabling the reproduction and characterization of distinct cell migratory patterns as a result of differences in matrix stiffness and cell metastatic potential.

1. Introduction

Cell migration plays a pivotal role in several physiological processes, such as tissue regeneration and embryonic development, and in pathological diseases such as cancer. In the context of cancer, metastasis involves a myriad of events during which cells disseminate from the primary tumor site and migrate to distant sites via neighboring blood and lymph vessels.[1–4] The first critical step of this cascade, invasion, is primarily influenced by the interactions between cells and their surrounding extracellular matrix (ECM).[5] Decades of research have revealed that tumor progression is not merely influenced by the underlying biochemical mechanisms, but it also involves ECM mechanics.[6] For example, tumor ECM mechanics depend on matrix stiffness, topography, and physical confinement, all of which can perpetuate the morphological abnormalities that lead to increased invasiveness and dissemination during the later stages of tumor evolution.[7–10] Moreover, in established medical procedures, tumors of the breast, lymph nodes, prostate, and thyroid are palpable as lumps because of an increased crosslinking density and disorderly arrangement of collagen fibers;[11,12] in addition, the enhancement of tumor stiffness is used as a biophysical indicator of cancer malignancy.[13] Although tissue stiffening as a result of cancer is a well-recognized process, the reciprocal influence of tissue stiffening on the regulation of cancer remains a topic to investigate.[14]

Efforts have been made to propagate cells from traditional 2D substrates to hydrogel based 3D artificial ECM mimics to better capture the pathophysiological features of tumors in vivo, such as gene expression profiles and drug responses.[15,16] The current strategies to mimic the biophysical nature of the natural ECM include the use of polymeric matrices, such as collagen, hyaluronic acid, fibronectin, Matrigel, gelatin, alginate, and poly(ethylene glycol),[17] in which multiple parameters such as porosity, polymer concentration, and matrix elasticity are simultaneously manipulated to capture tumor heterogeneity.[18–20] In particular, the role of stiffness is most often studied by tailoring the weight concentration of the prepolymer solution.[21,22] However, this also affects the density and pore size of the matrix.[23] As a result of these concurrent changes in multiple parameters and the divergence from physiological stiffening strategies, prior studies have hindered the attribution

J. Vasudevan, Prof. J. G. Fernandez
Engineering Product Development (EPD) Pillar
Singapore University of Technology and Design
8 Somapah Road, Singapore 487372, Singapore
E-mail: javier.fernandez@sutd.edu.sg
J. Vasudevan, Prof. C. T. Lim
Department of Biomedical Engineering
National University of Singapore
9 Engineering Drive 1, Singapore 117576, Singapore
Prof. C. T. Lim
Mechanobiology Institute
National University of Singapore
5A Engineering Drive 1, Singapore 117411, Singapore
Prof. C. T. Lim
Biomedical Institute for Global Health Research
and Technology (BIGHEART)
National University of Singapore
14 Medical Drive, Singapore 117599, Singapore
The ORCID identification number(s) for the author(s) of this article can be found under https://doi.org/10.1002/adfm.202005383.

DOI: 10.1002/adfm.202005383

of specific cell behaviors to matrix stiffness.[24,25] Therefore, to better understand how tumor cells "sense" their matrix and alter their migratory dynamics, it is necessary to develop physiologically relevant in vitro tumor-mimicking matrices, particularly ones where the stiffness level can be tuned in a biomimetic way (i.e., by intermolecular crosslinking) and independently of other parameters. These models can serve as viable tools for the development of novel therapeutic interventions that could help avert metastatic spread by directly targeting the mechanical niche-dependent mechanisms.

Gelatin methacrylate (GelMA) has been explored as an attractive hydrogel platform to fabricate in vitro tissue models owing to its biocompatibility, low cost, and ease of synthesis.[26] Derived from collagen, the major structural fibrous protein of the ECM, gelatin possesses arginyl-glycyl-aspartic acid sequences that facilitate integrin-mediated cell adhesion.[27] Recent demonstrations have indicated that GelMA is an attractive platform for building tumor models because the matrices promote cell adhesion, proliferation, and spreading.[28–30] As in other biopolymers, GelMA has been explored as a platform of tunable mechanical properties via the variation of the weight concentration of the prepolymer solution,[23,31] with concomitant variations of the stiffness,[32] ligand density,[33] and pore sizes.[34]

In contrast to previous studies, we mimic the biochemical and biophysical properties of natural tissue ECM by controlling the substitution of free amine groups of gelatin with methacrylic groups.[35] This controlled degree of methacryloyl functionalization (DoM) results in GelMA hydrogels that have finely tuned and physiologically relevant stiffness. To the best of our knowledge, this is the first use of ligand density alone as a biomimetic model of ECM stiffening processes and its application to determine the influence of ECM stiffness on cancer cell motility independent of other biophysical aspects of the local microenvironment.

GelMA-based artificial ECMs with elastic moduli ranging from 0.8 to 5 kPa were produced, matching the mechanical characteristics of a wide range of tissues, including that of normal and cancerous tissues.[36] The use of the artificial matrix was demonstrated by the photolithographic fabrication of a cell migration platform, whereby cells were embedded in patterned and controlled geometries and then surrounded by a cell-free hydrogel layer to create a 3D tumor-mimicking microenvironment. This chemical amendment and geometrical design of the artificial ECM helped map the varying migratory dynamics of tumor cells in noninvasive and invasive phenotypes. We believe the proposed biomimetic ECM and its associated stiffening mechanism could serve as a powerful tool to understand the role of tissue stiffening in the regulation of tumoral processes, to develop organ-on-chip platforms that will help unveil cell-matrix mechanoreciprocity in controlling cell migration phenomena, and to characterize the behavior of a specific tumoral explant for personalized medicine.

2. Results and Discussion

2.1. Evaluation of Gelatin Functionalization

We synthesized GelMA with different DoM by altering the amount of methacrylate (MA) added to the initial reaction, hence substituting the reactive amine groups on the gelatin chain (**Figure 1**a). This enabled fabrication of hydrogels of varying elasticities, ranging from the softest (≈50% DoM) to the stiffest (≈90% DoM). The gelatin:MA ratios were selected based on previous studies[37] (Figure S4a, Supporting Information), to match a range of stiffness levels with physiological relevance.[36] The nuclear magnetic resonance (^{1}H-NMR) characterization of GelMA revealed the successful substitution of amine groups on the parent gelatin that were directly proportional to the substitution ratio on the volume of MA in the initial reaction (Figure 1b). New signals were observed in GelMA at $\delta = 5.35$ ppm and $\delta = 5.6$ ppm, confirming the substitution of acrylic protons of the methacrylate functional groups (Figure 1c). With increasing amounts of MA added to the reaction, a continuous decrease in the signal was observed at $\delta = 2.9$ ppm, which corresponds to lysine methylene moieties (Figure 1d). A remarkable advantage of this localized substitution of amine groups by MA is that it enables the preservation of several functional amino acid moieties (Figure S4b, Supporting Information), thereby conserving the cell adhesion and thermal gelation properties of native gelatin molecules while precisely controlling for the number of sterically available MA groups and, consequently, the degree of intermolecular bonding.

2.2. Effect of DoM on Hydrogel Microstructure and Mechanical Properties

Hydrogels of varying elasticity, ranging from the softest (≈50% DoM) to the stiffest (≈90% DoM) were reconstructed using X-ray microtomography (μ-CT) (**Figure 2**a and Figure S5, Supporting Information). Due to the sub-micrometric size of the pores, well below the 8 μm resolution limit of the technique, we were unable to collect any quantitative information from this analysis.[38] A more accurate analysis using a scanning electron microscope (SEM) (Figure 2b) revealed an average pore diameter of about 90 nm in all samples, independent of the DoM (Figure 2c). These dimensions are far below the 1 μm^2 threshold values through which cells could breach and migrate into the matrix.[39] Despite the significant different mechanical properties of gels with different DoM, both qualitatively and statistically (Figure 2d), there were no statistically significant differences (p-value range = 0.06–0.3) in the pore sizes in all GelMA variants. During the formation of the hydrogels, the weight concentration—the main parameter currently used to alter the mechanical properties of hydrogels—defines the amount of solid phase with respect to the amount of liquid/void phase, and it is known to be the primary modulating parameter of the porosity.[40,41] In the model followed here, based on the physiological stiffening mechanism of the ECM, the stiffness varies uniquely from changes in the intermolecular bonding, which is precisely controlled by the DoM (Figure 2d–f), while the weight concentration and, therefore the porosity, was fixed at 10% w/v.

For all gels, the storage modulus values were several folds higher than the loss modulus values, thereby indicating a predominant elastic response, an observation that is in agreement with previous data.[42] The strength of GelMA variants, which is represented by their storage moduli (G'), revealed a direct

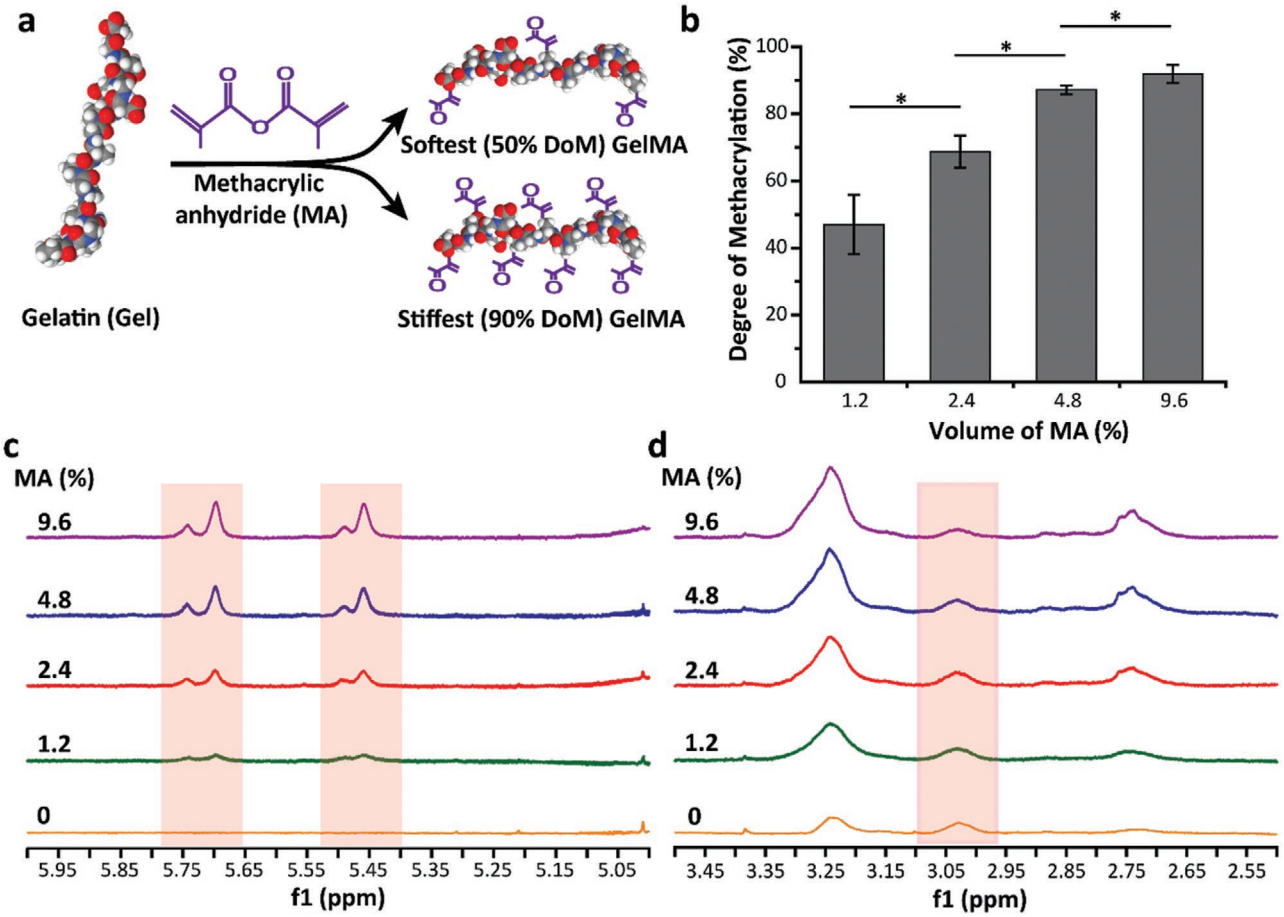

Figure 1. a) Synthesis of GelMA. Amino groups on gelatin (gel) were modified with methacrylate (MA) to form GelMA with varying degrees of substitution (softest ≈ 50%, stiffest ≈ 90%); b) quantification of DoM (%) using ^{1}H-NMR spectra; c) ^{1}H-NMR spectra: Chemical shifts indicating the presence of acrylic protons of methacrylate groups (5.35 ppm and 5.6 ppm); d) reduction of peak intensity of lysine methylene protons (≈ 2.9 ppm) with increasing DoM. Full spectra are available in Figure S4, Supporting Information.

correlation with their DoM and the ability of the proposed biomimetic stiffening mechanism to explore a wide range of physiologically relevant mechanical characteristics; *G'*s from as low as ≈500 Pa to as high as ≈5000 Pa were achieved, which can be correlated with that of numerous compliant natural tissues, such as brain, lung, or breast tissue (*G'* = 400–800 Pa), as well as other load-bearing tissues such as bone or muscle (*G'* = ≈2 kPa–2 GPa).[36,43,44]

In light of the results above, the proposed platform was not only able to mimic the stiffening process of natural ECM—based on crosslinking rather than density changes—but also match the mechanical values of native ECM, thereby providing physiological relevance for the study and control for cellular decisions such as viability, morphology, and migratory behavior based on substratum rigidity as an independent modulator. Moreover, because it is known that the progress of pathological conditions— specifically cancer—is associated with increased stiffness in the local microenvironment,[7,10] we tested the proposed combination of biomimetic ECM and stiffening mechanism for the production of a tumor-like microenvironment with controlled spatial (both for cell and material distributions) and mechanical characteristics.

2.3. Fabrication of MCF-7 and MDA-MB-231 Cell-Laden 3D Microenvironments with Variable Stiffness

Two variants of breast cancer cell lines—MCF-7 (noninvasive) and MDA-MB-231 (invasive)—were photo-crosslinked within 3D GelMA hydrogel systems of varying levels of stiffness to demonstrate the suitability of the proposed platform to recapitulate different cellular responses to the mechanics of the ECM. A graphical representation depicting the fabrication of the micropatterned tumor model is illustrated in **Figure 3**a. Briefly, cells were encapsulated in a densely packed cylindrical volume of 1 mm diameter and 400 µm height, which was surrounded by an acellular environment where cells could migrate. This configuration was chosen as the simplest reconstruction of a tumor tissue adjacent to a tumor-free environment. Additionally, it was designed with dimensions that could enable data acquisition at a single cell level within the range of several days of cellular displacements. It is noteworthy that this design was developed as a simple proof of concept to demonstrate the study of cell migration in well-defined heterogeneous environments using computer vision. More complex geometries were

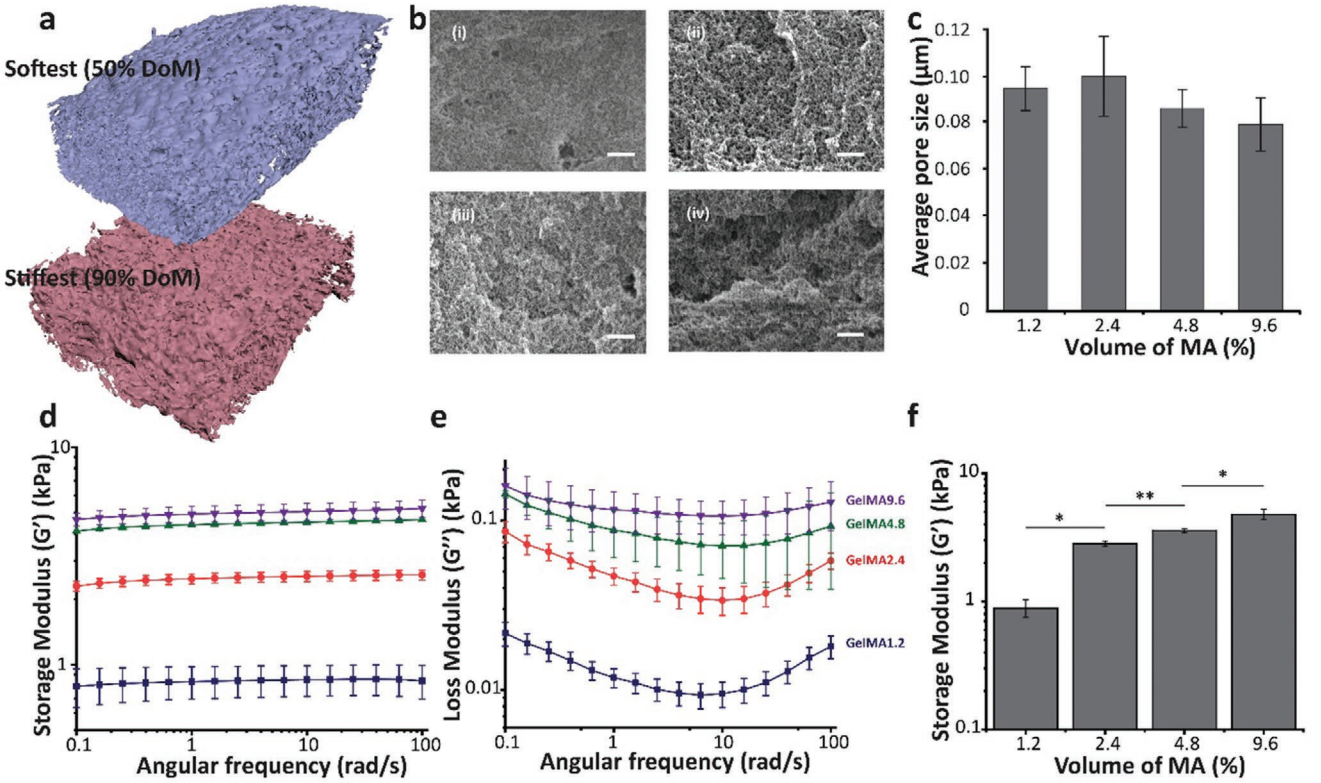

Figure 2. a) Volume rendering of reconstructed images obtained from μ-CT measurements (softest ≈ 50% DoM, stiffest ≈ 90% DoM) Volumes are approximately 2 × 2 × 1 mm. Due to resolution issues, pore sizes are largely overestimated; b) SEM micrographs of cross-sections of GelMA hydrogels with different DoM (%v/v) i) 1.2, ii) 2.4, iii) 4.8, and iv) 9.6. Scale bar = 1 μm; c) quantification of pore sizes based on SEM micrographs; rheological assessment of GelMA hydrogels with varying DoM d) storage moduli (*G'*) and e) loss moduli (*G''*) (plotted in the logarithmic scale); f) quantification of hydrogel elasticity at angular frequency = 10 rad s^{-1}.

produced to highlight the lack of constraints of the proposed system to simulate intricate tissue environments (Figure S6, Supporting Information).

The survival of cells in these matrices depends on various parameters, such as cell type, crosslinked volume, nutrient and gas diffusion, wavelength of ultraviolet (UV) light, and intensity of light utilized for photopolymerization. The two-step photopolymerization process did not have a substantial effect on the overall cell viability, thereby confirming the suitability of the material model as a platform for 3D cultures in the covered ranges of stiffness (Figure 3b,c). Interestingly, hydrogels with high methacrylation content showed higher cell viability compared with those with low methacryloyl content. Because all gels were radiated during the same time and power to keep the experimental conditions constant, this small difference in the viability of the gels with high DoM could be because of a greater number of functional groups absorbing energy and crosslinking at the expense of the radiation available to be absorbed by the embedded cells.[45] Additionally, the overall viabilities of the invasive MDA-MB-231 cells were significantly higher (89–99%) than that of MCF-7 cells (78–93%), confirming a variable degree of radiation resistance between cell types.[46–48]

Morphological adaptations of cells have been known to be dependent on matrix elasticity in both normal and disease mimicking microenvironments.[49–51] Here, cells embedded within the biomimetic ECMs of varying stiffness levels were found to be stably encapsulated and unaffected by the continuous replacements of the culture medium. The noninvasive MCF-7 cells displayed a round morphology within these patterned regions after a day of encapsulation (Figure 3d and Figure S7b–e, Supporting Information), a characteristic that was retained for the 5-day length of the experiment. Cellular clustering occurred in gels of lower elasticity (0.8 and 2.8 kPa), and it was observed to form after 48 h. The cluster size was also found to be positively correlated with time in gels of a lower stiffness value, whereas sizes were maintained at smaller dimensions in gels of a high stiffness level. This observation resonates with previous results, where MCF-7 cells have shown a rounded morphology and cluster formation in soft environments but exist mostly as single cells in gels of a high stiffness level.[49,52] The invasive MDA-MB-231 cells exhibited significantly better adaptation to the environment in the form of higher surface area (p-value = 0.00053) and aspect ratio (p-value = 2.53×10^{-8}) compared with MCF-7 cells (Figure 3e,f and Figure S7a,f–h, Supporting Information), with cell protrusions forming after day 2 of culture. These different morphologies between cell types became less significant as the stiffness of the surrounding ECM increased, and when the stiffness exceeded the physiological conditions of the breast tissue (i.e., >3.5 kPa), both MDA-MB-231 and MCF-7 showed a similar rounded morphology with no signs of an elongated cytoskeleton (Figure 3d,f). To the best of our knowledge, this is the first

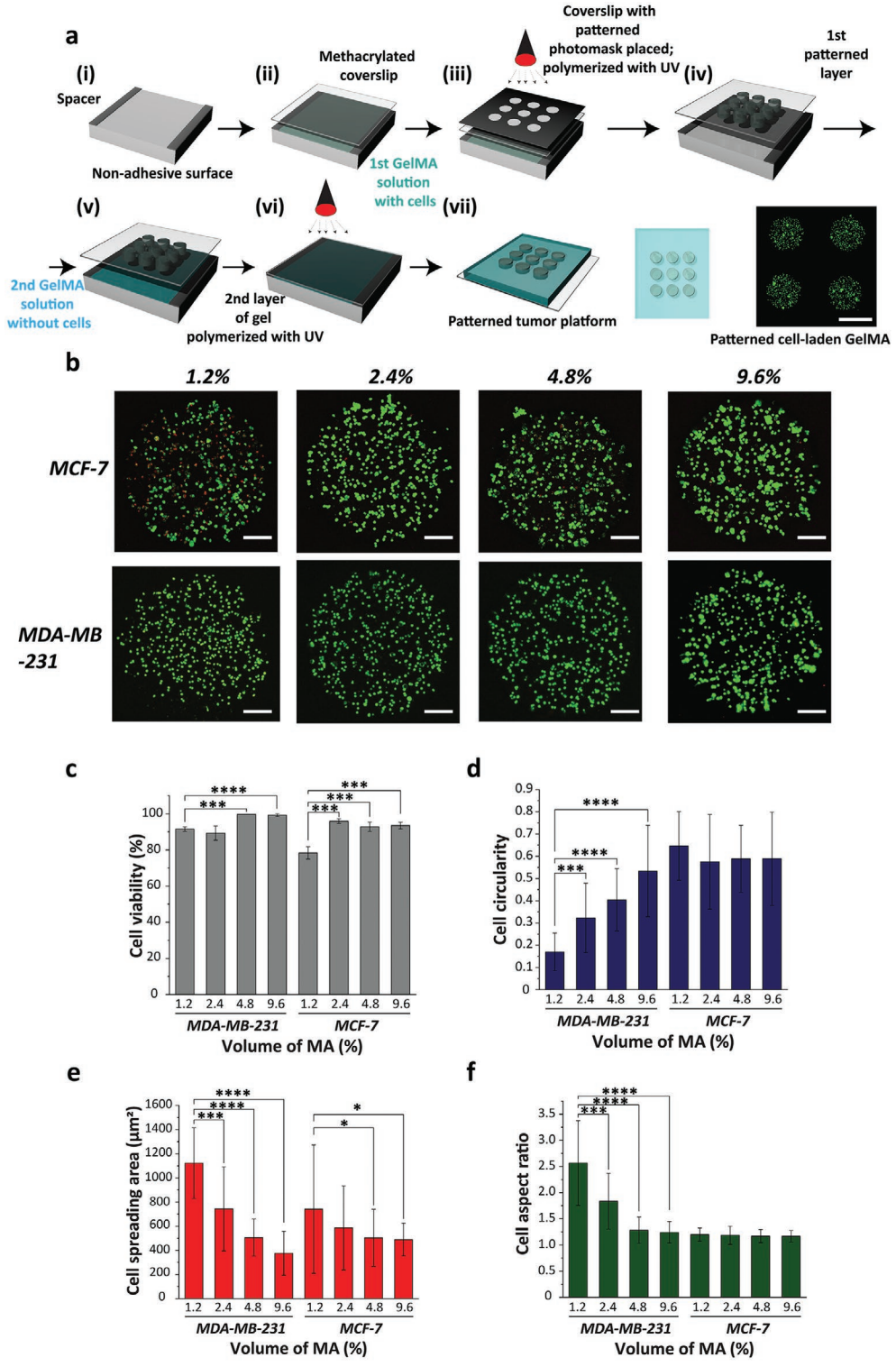

Figure 3. a) Illustration of the two-step photolithography process of fabrication of the tumor-mimicking platform. Cell-laden patterns are surrounded by cell-free hydrogel layer to provide free spaces for migration. Scale bar = 1 mm; b) cell viability analysis in cell-laden GelMA of varying stiffness and substitution degrees. Cells stained with calcein-AM (green)/ethidium homodimer (red) Live/Dead Assay 24 h after encapsulation (Scale bar = 200 µm); quantification of c) live cells in GelMA based on live/dead assay, d) cell circularity, e) cell spreading area, and f) cell aspect ratios based on images of cell morphological adaptations. Morphological measurements presented are representative of day 5 of culture within the hydrogels (average number of cells considered for quantifying cell morphology characteristics = 20 cells over 5 replicates). For comparison of cell morphology measurement trends over time refer Figure S7, Supporting Information. Lines over bars indicate that conditions were significantly different, as determined by ANOVA with $\alpha = 0.05$ ($^{*}p \leq 0.05$, $^{**}p \leq 0.01$, $^{***}p \leq 0.001$, $^{****}p \leq 0.0001$).

documentation of a differentiated adaptation of phenotypically different tumoral cells in response to a biomimetic change of the ECM stiffness alone, without changing other biophysical properties.

The different cellular adaptations of breast cancer cell models in environments of precisely defined mechanical and geometrical characteristics was a promising result of the applicability of the proposed biomimetic ECM and stiffening mechanism to reproduce physiological phenomena in a controlled manner. Subsequently, we explored the ability of the system to scrutinize and elucidate more complex, dynamic, and medically relevant cellular mechanisms, such as cell migration and cancer metastasis.

2.4. Cellular Migratory Behavior in GelMA as a Function of DoM

Cell migration within the biomimetic extracellular matrices of various stiffness levels was captured for a period of 24 h on days 1, 3, and 5 of culture using a live-cell microscopic imaging system and then analyzed using object tracking. We quantitatively compared the migratory properties at day 5 classified by cell displacements (i.e., Euclidean distance between the first and last point of the trajectory), track length (i.e., total displacement within the cell trajectory), path straightness (i.e., discrepancy between the cellular path and a straight line between the first and last migrating positions), and the mean cellular velocity (**Figure 4**). Some other magnitudes, such as relative cell migration with respect to the center of the gel (Figure S8, Supporting Information), were also collected but not analyzed because of their lack of an evident relationship with the purpose of the current study, which was to demonstrate the capability of the proposed ECM and stiffening models to successfully explore the mechanics of cell migration in breast cancer lines. A few examples of the raw data are included in Movies S1–S4, Supporting Information, as qualitative representations of the migratory aspects of these two cell types depending on the microenvironmental conditions.

Differences were observed in the time required by the cells to start migrating in environments of different stiffness levels; the cells embedded in soft gels showed a much earlier onset of cell migration (<48 h), whereas in highly rigid gel variants, migration was significantly impeded throughout the five days of experiment (Figures S9 and S10, Supporting Information). Two distinct modes of cell migration were observed in the system (Movie S5, Supporting Information); some cells displayed an amoeboid mode of migration, which was characterized by a round morphology and high levels of contractility. This migration mode was predominant in MCF-7. The rest of the cells adopted a mesenchymal migratory mode in which cell cytoskeletons were found to be polarized and elongated.[53–55] Mesenchymal migration was the preferred method for MDA-MB-231 cells. Overall, higher cellular displacements were observed in soft hydrogels (volume of MA: 1.2 and 2.4%) compared with gels with superior stiffness (volume of MA: 4.8 and 9.6%).

The engineered microenvironment successfully reproduced the different metastatic potentials of the two cell types utilized in the current study; phenotypically invasive MDA-MB-231 cells showed significantly higher displacements (1.2%: 18.01 ± 25.71 μm, 2.4%: 15.79 ± 16.18 μm) compared with noninvasive MCF-7 cells (1.2%: 5.069 ± 2.37 μm, 2.4%: 4.244 ± 2.52 μm) across all physiological stiffness levels (Figure 4b,c, Figures S9 and S10, Supporting Information). In the environment of lowest elasticity (volume of MA: 1.2%), the path lengths of the invasive cell line were almost 2 folds higher than those in stiffer matrices. This variation was not significant for the non-invasive MCF-7 cell line. In this stiffness level, MDA-MB-231 cells migrated at a significantly higher speed (p-value = 0.0102) that was 1.7 folds compared to MCF-7 cells (2.97 and 1.88 μm h^{-1}, respectively). Overall, cell migration speed in both cells was observed to be inversely related to the stiffness within the range of normal and tumoral breast tissue (p-value range = 2.4×10^{-4} to 3.09×10^{-6}), however no significant differences were observed beyond that range (Figure 4e, Figures S9 and S10, Supporting Information).

Stark differences were found on the track straightness (i.e., persistence) exhibited by the invasive MDA-MB-231 cells compared with the non-invasive MCF-7 cells (Figure 4d, Figures S9 and S10, Supporting Information); as with the trends in displacement, the differences in path persistence decreased with matrix stiffness. This general randomization of cell displacement, as a result of an environment that impedes movement, is similar to previous observations in high-density hydrogels.[56] The straighter and longer trajectories displayed by the mesenchymal phenotypes (MDA-MB-231) compared to those displayed by the epithelial phenotypes (MCF-7) closely resembles in vivo observations that may help explain the dynamics of the tumor invasion process.[57,58] Our results suggest that the differences on the cellular migration of the two cancer cell models examined are weakly related to the track length or speed of the cells, and strongly to the persistence (i.e., straightness) of their migration; in the physiological stiffness range of cancerous and healthy breast tissue, the highly invasive MDA-MB-231 migrates three times further away than the less invasive MCF-7 through a more directed migration.

Interestingly, in gels of low elasticity, a "scouting" behavior was observed, in which a few cells initiated an independent and direct migration into the surrounding cell-free environment to subsequently return to the cell-laden construct (Movie S6, Supporting Information). This interesting migratory pattern has been reported previously in MDA-MB-231.[30] Although rarer, we also observed it in the less invasive MCF-7. We can unequivocally confirm the existence of this phenomenon; however, because of the very limited previous reports on it, we are unable to hypothesize the mechanism behind it or its physiological relevance. Nevertheless, we believe that, given the specific conditions reported here for its reproduction, the study of such a mechanism could be an immediate follow-up application of the biomimetic platform presented here.

3. Conclusion

We proposed, characterized, and evaluated the use of the degree of methacrylation of photo-crosslinkable GelMA as a biomimetic model of stiffening in the ECM. We later applied these results to explore the role of the stiffness level of the local microenvironment in regulating breast cancer cell migration. Using photolithography, breast cancer cells were compartmentalized by embedding them in circular constructs and surrounding them with a cell-free hydrogel layer, a configuration

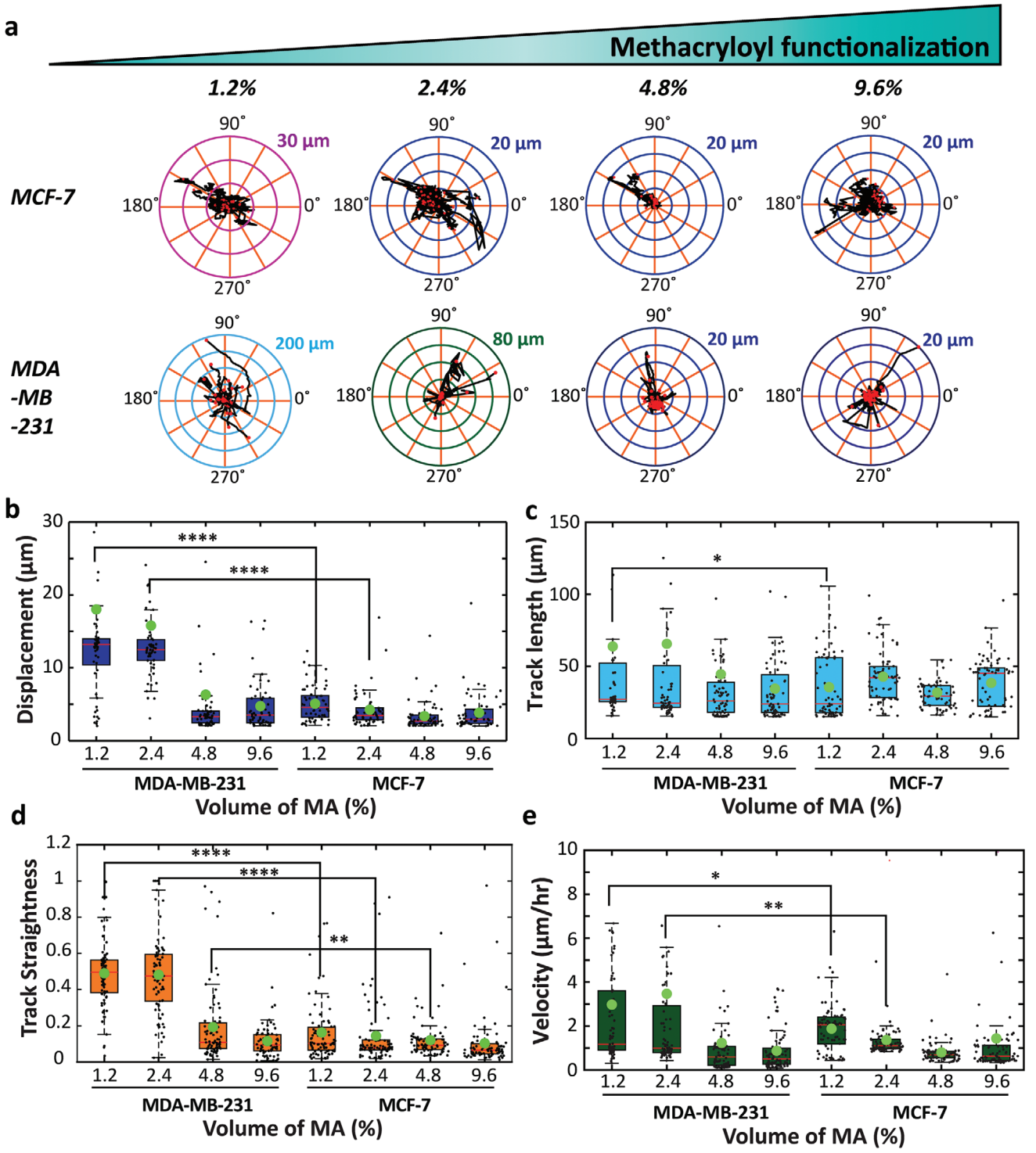

Figure 4. Migratory behavior controlled by matrix stiffness and GelMA substitution degree: a) MCF-7 and MDA-MB-231 single cell trajectories cultured in GelMA hydrogel variants; tracks were normalized with respect to the origin; b) scatterplot and box plot comparison of cell track displacements; c) quantified cell path lengths; d) scatterplot and box plot comparison of cellular track straightness indices. e) Scatterplot and box plot comparison of migration velocities. Measurements presented are representative are at day 5 of culture (average number of cells = 80 cells per migration measurement averaged over five replicates; for a comparison of cell migratory measurement trends over time, refer to Figures S9 and S10, Supporting Information; for a complete list of statistical significance refer to Figure S11, Supporting Information). Green markers represent average values. In the box plots, the middle line indicates median, the top and bottom of the box indicate the 75th and 25th percentiles, respectively, and the whiskers indicate the 90th and 10th percentiles. Lines over bars indicate that conditions were statistically significantly different as determined by ANOVA with $\alpha = 0.05$ (*$p \leq 0.05$, **$p \leq 0.01$, ***$p \leq 0.001$, ****$p \leq 0.0001$). Black round markers outside the plot indicate that there are values that lie beyond the range of the y-axis.

specifically designed to simultaneously provide physiological relevance and facilitate data acquisition. The proposed system enabled the fine tuning of the stiffness of hydrogel matrices independently of other parameters, such as density or porosity, with outstanding granularity and natural resemblance. Regardless of the degree of functionalization, high cell viabilities were observed, while differential adaptations and migration modes were observed regarding both cancer cell type and the surrounding biophysical conditions. The ability to manipulate hydrogel mechanics using the DoM substitution can help find the "Goldilocks window" for designing optimal hydrogel-based tissue mimics for understanding cell-matrix mechano-reciprocity in both normal and diseased conditions. To this end, the proposed biomimetic ECM and stiffening mechanism can help provide an inspiring opportunity to develop novel studies and therapeutic interventions that can specifically and independently target the mechanical features of the microenvironment.

4. Experimental Section

Synthesis of GelMA: Gelatin (Type A, 300 bloom from porcine skin, Sigma Aldrich) was mixed at 10% (w/v) into 1X-Dulbecco's Phosphate Buffered Saline (1X D-PBS, Nacalai Tesque) at 55 °C and stirred until fully dissolved. Methacrylic anhydride (MA, Sigma Aldrich) was added in a dropwise manner at the rate of 100 µL min^{-1} to the gelatin solution under stirred conditions and allowed to react in the dark for 2 h. Four batches of GelMA with a varying DoM were synthesized by varying the amount of MA added to the initial reaction. The GelMA solution was transferred to tubes and centrifuged at 3500 G for 3 min at room temperature. The unreacted MA forms the pellet and the GelMA solution is collected as the supernatant. The supernatant is diluted to two volumes of preheated 1X D-PBS (37 °C) and then subjected to dialysis against distilled water (MWCO 12–14 kDa, SpectraPor) for 1 week at 50 °C to remove the remaining salts and unreacted methacrylic acid groups. Fresh distilled water was replaced twice a day during the dialysis process. The solutions were filtered, frozen at −80 °C overnight and lyophilized to generate white porous foam. The samples were stored at −20 °C until further experiments.

Quantification of GelMA DoM: The DoM of GelMA variants was verified using ^{1}H-NMR spectra (Bruker AVIII HD equipped with a BBFO probe) collected at 37 °C at a frequency of 400 MHz. Around 10 mg of lyophilized gelatin and GelMA samples were dissolved in 1 mL of deuterium oxide (D_2O) (Cambridge Isotope Laboratories, Inc.). Phase correction was applied to obtain purely absorptive peaks. Baseline correction was applied before obtaining the areas (integrals) of the peaks of interest. The spectra were normalized to the peak indicating phenylalanine (6.9–7.4 ppm). Subsequently the lysine-methylene signals (2.8–2.95 ppm) were integrated to obtain the areas. The DoM of different batches of GelMA were calculated as

$$\mathrm{DoM}(\%) = \left[1 - \frac{\mathrm{area(lysine-methylene\ signals\ of\ GelMA}}{\mathrm{area(lysine-methylene\ signals\ of\ gelatin}}\right] \times 100 \quad (1)$$

Rheological Characterization of GelMA Hydrogels: 0.5% (w/v) 2-hydroxy-1-(4-(hydroxyethoxy) phenyl)-2-methyl-1-propanone (Irgacure 2959, Sigma Aldrich) as a photoinitiator was fully dissolved in 1X D-PBS at 80 °C. This solution was cooled down to 50 °C prior to adding the freeze dried GelMA macromer at a concentration of 10% (w/v). 1.2 mL of this prepolymer solution was cast into a circular mold of 25 mm diameter. The polymer solution was placed 8 cm away from the light source and exposed to 1.35 W cm^{-2} UV light (320–500 nm) for 60 s. The gels were incubated in 1X D-PBS for 24 h at 37 °C overnight. Rheological assessment was performed using a rheometer equipped with parallel plate geometry (HR-2 Discovery Hybrid Rheometer, TA instruments using a 20-mm diameter parallel plate). The edges of hydrogel discs were trimmed to fit the 20-mm parallel plate geometry. A constant gap of 0.7 mm was maintained between the samples and parallel plate throughout the entire experiment. A strain sweep measurement was first conducted with strain amplitude γ = 0.1–100% and fixed frequency f = 1 Hz to determine the linear regime of γ. Oscillating frequency sweeps were performed at room temperature (25 °C) with constant frequency (1 Hz) and strain rate (10%). The storage and loss modulus were continuously recorded using the TRIOS software. Analysis was performed for at least three replicate samples of each GelMA variant.

Morphological Assessment of GelMA Hydrogels: The ultrastructure of the hydrogel variants was analyzed using Scanning Electron Microscopy (SEM) (JEOL JSM 7600F, Peabody, MA, USA). Upon fabrication, the hydrogels were washed thoroughly with 1X D-PBS. Then, they were dehydrated in a gradient manner using a series of ethanol concentrations: 1 × 24 h in 25%, 50%, 75%, 95% concentration each followed by 3 × 72 h in 100% ethanol. Following gradient drying, the samples were subjected to critical point drying (Leica EM CPD300) for 5 h. Samples were cut into thin sections and placed on double-sided carbon tape, attached to a metal surface and sputter-coated with gold for 40 s. SEM micrographs were acquired at 15 000 X magnification under vacuum conditions at room temperature (25 °C). Pore diameters were quantified using ImageJ software (National Institute of Health (NIH), USA). Images of three independent sets of samples for each hydrogel were binarized and pore sizes were measured manually (n = 10).

X-Ray Microcomputed Tomography (µ-CT) Analysis: Radiopacity measurements of dried GelMA scaffolds of different DoM was carried out using Skyscan 1076 (Bruker, Kontich, Belgium) micro CT (µCT) system using the following settings: 64 kV operational source voltage, 155 µA source current, 1178 ms exposure time and 8.87 µm pixel size. Reconstruction of the projected images was performed using NRecon (Skyscan, Kontich, Belgium) software and analyzed using CT Analyzer (CTAN, Bruker, Kontich, Belgium). 3D reconstructions were rendered using 3D Studio (Autodesk Inc, USA)

Cell Culture: Non-invasive (MCF-7) and invasive (MDA-MB-231) human breast adenocarcinoma cell lines (MCF-7) were used in this study. Both cell lines were cultured and maintained in Dulbecco's Modified Eagles Medium (DMEM, high glucose) supplemented with 10% v/v fetal bovine serum (FBS, Life Technologies) and 1% v/v Penicillin-Streptomycin mixed solution (Nacalai Tesque). Cells were maintained at normal physiological conditions (37 °C, 5% CO_2), passaged every three days, and their media was replenished every two days.

Fabrication of 3D Cell Embedding Hydrogels: Micropatterned hydrogels embedding cells were fabricated using the process of photolithography as previously described.[30] Glass coverslips were washed extensively in different solvents in the following order: deionized water, acetone, and ethanol (100%) for a period of 30 min in each solvent. They were dried overnight at 60 °C and then subjected to functionalization with 3-(Trimethoxysilyl) propyl methacrylate (TMSPMA, Sigma-Aldrich) using vapor deposition method to facilitate optimal adhesion of GelMA hydrogel constructs on glass substrates. In order to ensure successful deposition of TMSPMA, a water droplet was pipetted onto untreated and treated glass surfaces. Contact angle measurements (Figure S1a,b, Supporting Information) were performed on this water droplet using the Contact Angle plugin for ImageJ (NIH public domain software). After silanization, the coverslips were baked at 100 °C for 1 h and stored until further experiments.

To prevent cells from attaching and invading on the coverslip, 50 µL of 20% (w/v) Polyethylene glycol dimethacrylate (PEGDMA, Polysciences Inc.) polymer solution containing 0.5% (w/v) Irgacure 2959 was pipetted onto a non-adhesive Petri dish. The working distance between the light source and coverslip was set to be 8 cm. The silanized coverslip is inverted on to the PEGDMA solution and exposed to UV light (360–480 nm, 1.35 W cm^{-2}) for 60 s to form a thin layer of PEGDMA coating on top of the TMSPMA-treated glass coverslips. 10% (w/v) of freeze-dried GelMA was dissolved DMEM containing 0.5% (w/v) Irgacure 2959. Once the cells reach confluency, they were trypsinized using 0.25%-Trypsin/1mM-EDTA

solution (Nacalai Tesque), centrifuged, and resuspended in the GelMA solution at a concentration of 2×10^6 cells mL^{-1} of GelMA. The tumor model was first patterned by pipetting 200 µL of cell-laden GelMA solution onto a non-adhesive Petri dish flanked by spacers of depth 0.4 mm. The PEGDMA coated coverslip is inverted on top of this cell/GelMA mixture to spread it evenly to cover the area and fill the spacer depth. A negative acetate photomask (designed using AutoCAD and printed at 25 000 dpi resolution using an ink-jet printer by Great Lakes Engineering, USA) was placed on top of this coverslip. The photomask (Figure S2a,b, Supporting Information) had a layout of four transparent circles of diameter 1 mm surrounded by a black unpatterned area. The distance between circles was 3 mm. After UV exposure (1.35 W cm^{-2}, 30 s), the patterned coverslip was washed thoroughly with warm 1X D-PBS to remove the remaining uncrosslinked polymer, revealing circular cell-laden crosslinked GelMA constructs. Next, 200 µL of pure GelMA solution (without cells) was pipetted onto the spacer and coverslip was inverted onto this prepolymer solution. This setup was again exposed to UV light (1.35 W cm^{-2}, 30 s) to crosslink the gel surrounding the cell-laden construct. The cell-laden patterns were glued to 6 well culture plates and washed in warm 1X D-PBS to remove any traces of uncrosslinked polymer. Finally, they were cultured by supplementing with DMEM and placed in an incubator (37 °C, 5% CO_2). Fresh culture medium was replenished every day over the course of experiments.

Cell Viability and Morphometric Analysis: Cell viability analysis was performed after 24 h using Live/Dead viability/cytotoxicity kit (InvitrogenTM) that contained calcein-AM (calcein) and ethidium homodimer (EthD-1). 20 µL of 2mM EthD-1 and 5 µL of 4mM calcein was added to 10 mL of 1X D-PBS and vortexed thoroughly. This serves as stock solution. Gels were rinsed thoroughly in warm 1X D-PBS and 150 µL of live/dead stock solution was added. The coverslips were stored at physiological conditions (37 °C, 5% CO_2) for 45 min, followed by imaging using an inverted microscope (Zeiss Axio Observer D1, 5X (0.15 N.A) and 10X (0.25 N.A) magnifications). Images were taken using green fluorescence channel for live cells and red fluorescence channel for dead cells. The number of green and red fluorescent cells was quantified using ImageJ. The percentage viability for triplicate sample sets was calculated by dividing the number of live cells (green) to the total number of cells (green and red).

To measure the morphological features of different GelMA variants, the cells were cultured within the 3D gels and imaged every day for a total of 5 days. Brightfield images were taken using an optical microscope (Olympus IX 81 inverted microscope) with MetaMorph software at 10X (0.30 N.A) magnification. The characterization of cells for morphology and for migration purposes was made at a distance of at least 50 µm from the bottom of the gel, to avoid collecting data from cells close to the PEGDMA-GelMA interface. Single cells were segmented and analyzed on ImageJ (NIH public domain software) using Shape Descriptor Macros. For accuracy, cell clusters were not included in this analysis. To quantify the differences in morphology, the major and minor axis of the cell cytoskeleton were measured using a scale bar in the ImageJ software. The cell spreading area and perimeter were evaluated. The circularity and aspect ratio were calculated as:

$$\text{Circularity} = 4\pi^* \frac{\text{Area of the cell}}{(\text{Perimeter of the cell})^2} \quad (2)$$

$$\text{Aspect Ratio} = \frac{\text{Major axis}}{\text{Minor axis}} \quad (3)$$

Circularity formula provides a value between 0 and 1. Values above 0.5 indicate rounded cells and values below 0.5 indicate elongated cells. At least twenty cells were analyzed from triplicate samples.

Assessment of Cell Migratory Behavior: Cell- laden hydrogel patterns were cultured for 24 h prior to time-lapse experiments. Imaging was carried out using a microscope (Olympus IX 81 inverted microscope) equipped with a software controlled motorized stage and an incubation system to maintain cells under physiological conditions (37 °C, 5% CO_2) and perform imaging at several positions. Phase contrast images were obtained at 10X (0.30 N.A) magnification to image each cell-laden circular pattern and acellular surrounding area in a single field-of-view. Imaging was performed at about 100 µm within the construct to track cell migration within the 3D GelMA. The cells were imaged every 20 min for three 24 h time intervals (25–48 h, 73–96 h, and 121–144 h). Cells were tracked in circular construct for a total of 5 constructs per combination of cell type and DoM. A minimum of 80 cell tracks per cell/DoM combination were included in the analysis. Cell tracking analyses were quantified using a built-in tracking algorithm in Imaris software (Bitplane, Zurich, Switzerland) with close human supervision. Contrast enhancement, image segmentation, and drift correction were performed prior to analysis. Tracks lost in less than 6000 s were eliminated as they were resulting from object identification errors. The vast majority of the tracks recorded covered from frame 1 till the end (i.e., 24 h). In some few instances, new cells were identified and tracked at later stages. Those new tracks registered for more than 6000 s were included in the kinematic analysis as they were instances of cell division or cells traveling vertically into the focal plane. In addition, live imaging was performed on red fluorescence beads (10 µm) embedded in all GelMA variants for a period of 24 h to categorize secondary motion effects. Based on their tracking data (Figure S3, Supporting Information), paths of less than 15 µm in 24 h could not be unequivocally assigned to cell migration and they were discarded from the analysis. Cell migration parameters such as displacement, velocity, path lengths, and track straightness were evaluated at each of the three 24 h time periods (i.e., days 1, 3, and 5). Displacement was defined as the length of the vector directly connecting the start and end of the cell paths. Velocity was calculated as the average cell displacement over each time interval of a given path. Track length is defined as the total length of displacements within the track. Track straightness is the ratio of cell displacement to path length. All calculations, analysis, and graphical representations were made using MATLAB (Mathworks, Natick, MA).

Statistical Analysis: All data were presented as mean ± deviation (SD). A one-way analysis of variance (ANOVA) was conducted to validate statistically significant differences between the GelMA variants when $\alpha = 0.05$.

Supporting Information

Supporting Information is available from the Wiley Online Library or from the author.

Acknowledgements

This work was supported by the Singapore University of Technology and Design (SUTD), the Mechanobiology Institute (MBI) and the Mechanobioengineering (MBE) Lab at the National University of Singapore (NUS).

Conflict of Interest

The authors declare no conflict of interest.

Author Contributions

J.G.F. and C.T.L. conceived and supervised the project; J.V. performed research; J.V., J.G.F., and C.T.L. wrote the manuscript.

Keywords

biological materials, cancer cell migration, Gelatin methacrylate, porous materials, stiffness, tissue models

Received: June 25, 2020
Revised: August 13, 2020
Published online:

[1] C. L. Chaffer, R. A. Weinberg, *Science* **2011**, *331*, 1559.
[2] Q. K. Chen, K. Lee, D. C. Radisky, C. M. Nelson, *Differentiation* **2013**, *86*, 126.
[3] Y. Yu, C. H. Xiao, L. D. Tan, Q. S. Wang, X. Q. Li, Y. M. Feng, *Br. J. Cancer* **2014**, *110*, 724.
[4] J. E. Talmadge, I. J. Fidler, *Cancer Res.* **2010**, *70*, 5649.
[5] L. A. Liotta, *Cancer Res.* **2016**, *76*, 3115.
[6] K. M. Wisdom, K. Adebowale, J. Chang, J. Y. Lee, S. Nam, R. Desai, N. S. Rossen, M. Rafat, R. B. West, L. Hodgson, O. Chaudhui, *Nat. Commun.* **2018**, *9*, 4144.
[7] S. Kumar, A. Pathak, *Integr. Biol.* **2013**, *5*, 1067.
[8] X. Sun, D. J. Glynn, L. J. Hodson, C. Huo, K. Britt, E. W. Thompson, L. Woolford, A. Evdokiou, J. W. Pollard, S. A. Robertson, W. V. Ingman, *Breast Cancer Res.* **2017**, *19*, 4.
[9] M. G. Rubashkin, L. Cassereau, R. Bainer, C. C. DuFort, Y. Yui, G. Ou, M. J. Paszek, M. W. Davidson, Y. Y. Chen, V. M. Weaver, *Cancer Res.* **2014**, *74*, 4597.
[10] K. R. Levental, H. Yu, L. Kass, J. N. Lakins, M. Egeblad, J. T. Erler, S. F. T. Fong, K. Csiszar, A. Giaccia, W. Weninger, M. Yamauchi, D. L. Gasser, V. M. Weaver, *Cell* **2009**, *139*, 891.
[11] O. Brouckaert, A. Schoneveld, C. Truyers, E. Kellen, C. Van Ongeval, I. Vergote, P. Moerman, G. Floris, H. Wildiers, M. R. Christiaens, E. Van Limbergen, P. Neven, on behalf of MBC Leuven, Belgium, *Ann. Oncol.* **2013**, *24*, 1847.
[12] B. Ahn, E. I. S. Lorenzo, K. H. Rha, H. J. Kim, J. Kim, *J. Endourol.* **2011**, *25*, 851.
[13] B. Emon, J. Bauer, Y. Jain, B. Jung, T. Saif, *Comput. Struct. Biotechnol. J.* **2018**, *16*, 279.
[14] M. W. Pickup, J. K. Mouw, V. M. Weaver, *EMBO Rep* **2014**, *15*, 1243.
[15] E. L. S. Fong, T. B. Toh, X. Lin, Z. Liu, L. Hooi, M. B. Mohd Abdul Rashid, T. Benoukraf, E. K. H. Chow, T. H. Huynh, H. Yu, *Biomaterials* **2018**, *159*, 229.
[16] C. Curtin, J. C. Nolan, R. Conlon, L. Deneweth, C. Gallagher, Y. J. Tan, B. L. Cavanagh, A. Z. Asraf, H. Harvey, S. Miller-Delaney, J. Shohet, I. Bray, F. J. O'Brien, R. L. Stallings, O. Piskareva, *Acta Biomater* **2018**, *70*, 84.
[17] I. M. El-Sherbiny, M. H. Yacoub, *Glob. Cardiol. Sci. Pract.* **2013**, *2013*, 38.
[18] J. Sapudom, S. Rubner, S. Martin, T. Kurth, S. Riedel, C. T. Mierke, T. Pompe, *Biomaterials* **2015**, *52*, 367.
[19] C. Wang, X. Tong, F. Yang, *Mol. Pharm.* **2014**, *11*, 2115.
[20] S. Pradhan, I. Hassani, W. J. Seeto, E. A. Lipke, *J. Biomed. Mater. Res. - Part A* **2017**, *105*, 236.
[21] V. L. Cross, Y. Zheng, N. Won Choi, S. S. Verbridge, B. A. Sutermaster, L. J. Bonassar, C. Fischbach, A. D. Stroock, *Biomaterials* **2010**, *31*, 8596.
[22] M. G. Haugh, C. M. Murphy, R. C. McKiernan, C. Altenbuchner, F. J. O'Brien, *Tissue Eng. - Part A* **2011**, *17*, 1201.
[23] A. Pathak, S. Kumar, *Proc. Natl. Acad. Sci. U. S. A.* **2012**, *109*, 10334.
[24] B. N. Mason, A. Starchenko, R. M. Williams, L. J. Bonassar, C. A. Reinhart-King, *Acta Biomater* **2013**, *9*, 4635.
[25] Y. Li, M. J. Fanous, K. A. Kilian, G. Popescu, *Sci. Rep.* **2019**, *9*, 248.
[26] J. W. Nichol, S. T. Koshy, H. Bae, C. M. Hwang, S. Yamanlar, A. Khademhosseini, *Biomaterials* **2010**, *31*, 5536.
[27] B. J. Klotz, D. Gawlitta, A. J. W. P. Rosenberg, J. Malda, F. P. W. Melchels, *Trends Biotechnol.* **2016**, *34*, 394.
[28] A. D. Arya, P. M. Hallur, A. G. Karkisaval, A. Gudipati, S. Rajendiran, V. Dhavale, B. Ramachandran, A. Jayaprakash, N. Gundiah, A. Chaubey, *ACS Appl. Mater. Interfaces* **2016**, *8*, 22005.
[29] A. Aung, J. Theprungsirikul, H. L. Lim, S. Varghese, *Lab Chip* **2016**, *16*, 1886.
[30] N. Peela, F. S. Sam, W. Christenson, D. Truong, A. W. Watson, G. Mouneimne, R. Ros, M. Nikkhah, *Biomaterials* **2016**, *81*, 72.
[31] A. J. Berger, K. M. Linsmeier, P. K. Kreeger, K. S. Masters, *Biomaterials* **2017**, *141*, 125.
[32] X. Tang, T. B. Kuhlenschmidt, J. Zhou, P. Bell, F. Wang, M. S. Kuhlenschmidt, T. A. Saif, *Biophys. J.* **2010**, *99*, 2460.
[33] M. H. Zaman, L. M. Trapani, A. L. Sieminski, D. MacKellar, H. Gong, R. D. Kamm, A. Wells, D. A. Lauffenburger, P. Matsudaira, *Proc. Natl. Acad. Sci.* **2006**, *103*, 10889.
[34] Y. L. Yang, S. Motte, L. J. Kaufman, *Biomaterials* **2010**, *31*, 5678.
[35] B. H. Lee, H. Shirahama, N. J. Cho, L. P. Tan, *RSC Adv.* **2015**, *5*, 106094.
[36] T. R. Cox, J. T. Erler, *Dis. Model. Mech.* **2011**, *4*, 165.
[37] D. Loessner, C. Meinert, E. Kaemmerer, L. C. Martine, K. Yue, P. A. Levett, T. J. Klein, F. P. W. Melchels, A. Khademhosseini, D. W. Hutmacher, *Nat. Protoc.* **2016**, *11*, 727.
[38] S. Peng, Q. Hu, S. Dultz, M. Zhang, *J. Hydrol.* **2012**, *472–473*, 254.
[39] K. Wolf, M. te Lindert, M. Krause, S. Alexander, J. te Riet, A. L. Willis, R. M. Hoffman, C. G. Figdor, S. J. Weiss, P. Friedl, *J. Cell Biol.* **2013**, *201*, 1069.
[40] X. Zhao, Q. Lang, L. Yildirimer, Z. Y. Lin, W. Cui, N. Annabi, K. W. Ng, M. R. Dokmeci, A. M. Ghaemmaghami, A. Khademhosseini, *Adv. Healthcare Mater.* **2016**, *5*, 108.
[41] J. Yin, M. Yan, Y. Wang, J. Fu, H. Suo, *ACS Appl. Mater. Interfaces* **2018**, *10*, 6849.
[42] E. Hoch, C. Schuh, T. Hirth, G. E. M. Tovar, K. Borchers, *J. Mater. Sci. Mater. Med.* **2012**, *23*, 2607.
[43] T. A. Krouskop, T. M. Wheeler, F. Kallel, B. S. Garra, T. Hall, *Ultrason. Imaging* **1998**, *20*, 260.
[44] J. M. Barnes, L. Przybyla, V. M. Weaver, *J. Cell Sci.* **2017**, *130*, 71.
[45] M. Zhu, Y. Wang, G. Ferracci, J. Zheng, N. J. Cho, B. H. Lee, *Sci. Rep.* **2019**, *9*, 6863.
[46] H. Saini, A. Navaei, A. Van Putten, M. Nikkhah, *Adv. Healthcare Mater.* **2015**, *4*, 1961.
[47] J. Kim, C. M. Hope, N. Gantumur, G. B. Perkins, S. O. Stead, Z. Yue, X. Liu, A. U. Asua, F. D. Kette, D. Penko, C. J. Drogemuller, R. P. Carroll, S. C. Barry, G. G. Wallace, P. T. Coates, *Adv. Funct. Mater.* **2020**, *30*, 2000544.
[48] J. W. Nichol, S. T. Koshy, H. Bae, C. M. Hwang, S. Yamanlar, A. Khademhosseini, *Biomaterials* **2010**, *31*, 5536.
[49] M. Cavo, M. Fato, L. Peñuela, F. Beltrame, R. Raiteri, S. Scaglione, *Sci. Rep.* **2016**, *6*, 35367.
[50] M. Ehrbar, A. Sala, P. Lienemann, A. Ranga, K. Mosiewicz, A. Bittermann, S. C. Rizzi, F. E. Weber, M. P. Lutolf, *Biophys. J.* **2011**, *100*, 284.
[51] J. E. Kim, D. S. Reynolds, M. H. Zaman, M. Mak, *Integr. Biol.* **2018**, *10*, 232.
[52] S. Krause, M. V. Maffini, A. M. Soto, C. Sonnenschein, *BMC Cancer* **2010**, *10*, 263.
[53] K. Paňková, D. Rösel, M. Novotný, J. Brábek, *Cell. Mol. Life Sci.* **2010**, *67*, 63.
[54] J. Zhu, A. Mogilner, *Interface Focus* **2016**, *6*, 20160040.
[55] Y. J. Liu, M. Le Berre, F. Lautenschlaeger, P. Maiuri, A. Callan-Jones, M. Heuzé, T. Takaki, R. Voituriez, M. Piel, *Cell* **2015**, *160*, 659.
[56] W. Sun, C. T. Lim, N. A. Kurniawan, *J. R. Soc. Interface* **2014**, *11*, 20140638.
[57] W. Wang, J. B. Wyckoff, V. C. Frohlich, Y. Oleynikov, S. Hüttelmaier, J. Zavadil, L. Cermak, E. P. Bottinger, R. H. Singer, J. G. White, J. E. Segall, J. S. Condeelis, *Cancer Res.* **2002**, *62*, 6278.
[58] F. Ahmed, J. Wyckoff, E. Y. Lin, W. Wang, Y. Wang, L. Hennighausen, J. ichi Miyazaki, J. Jones, J. W. Pollard, J. S. Condeelis, J. E. Segall, *Cancer Res.* **2002**, *62*, 7166.